УДК 621.382.592 DOI: 10.15222/TKEA2026.1.17

Ihor VIRT, Ivan PADALKA

Ukraine, Ivan Franko State Pedagogical University of Drohobych

MODELING OF A PHOTODIODE STRUCTURE BASED ON A HETEROJUNCTION ZnO/Si

In this work, a self-powered photodetector based on a bulk ZnO/Si p–n heterojunction is numerically investigated and analyzed using the Solar Cell Capacitance Simulator in One Dimension (SCAPS-1D). The energy band diagram, electron-hole generation and recombination rates, current-voltage (J–V) characteristics, spectral photosensitivity response, and specific detectivity are examined. To optimize photodetector performance, the effects of absorber layer thickness, shallow acceptor and donor densities, and defect density were systematically studied. Various electron transport parameters of ZnO were also considered. The responsivity and specific detectivity of the simulated photodetector are 0.23 A/W and $1.1 \cdot 10^{10}$ Jones, respectively.

Keywords: photovoltaic cell, photodetector, numerical simulation, electron transport material (ETM), ZnO, heterostructure, SCAPS-1D program.

Current trends in sensor instrumentation encompass a range of promising emerging technologies alongside innovative chemical and physical processes, as well as advanced systems for signal generation, conversion, and transmission. Photodetectors, which directly convert light into electrical signals, have been developed for numerous applications, including medical diagnostics, aviation, target recognition, and related fields [1]. Self-powered photodetectors based on *p–n* junctions exhibit outstanding photovoltaic characteristics—such as fast response speed, wide linear dynamic range, and low noise—and have demonstrated significant progress in recent years [2]. To further enhance these parameters, research groups are developing dedicated simulation tools and conducting photovoltaic device modeling studies. Simulation methods provide valuable insight into the physical phenomena governing photovoltaic cell operation. For this purpose, SCAPS-1D (Solar Cell Capacitance Simulator—One Dimensional) software has been widely adopted [3].

The built-in electric field present at the heterojunction interface between dissimilar materials acts as a driving force for the efficient separation of photogenerated charge carriers, thereby sustaining a continuous photocurrent. When electron-hole pairs are generated within the depletion region of a *p–n* junction, the local electric field separates them, allowing the carriers to be collected at the respective external contacts.

Currently, theoretical studies of silicon-based heterostructures are widely conducted using SCAPS software. In particular, planar configurations of metal oxides and silicon, such as ZnO/Si, are commonly employed as model systems. Numerical analysis is performed to determine the optimal conditions for such photodetectors, and the factors governing their performance are systematically investigated. Numerical modeling represents a critically important stage in optimizing device architectures prior to experimental fabrication and testing. Furthermore, simulation results demonstrate that well-aligned energy bands in the metal oxide and silicon lead to improved device performance, whereas misalignment of the bands results in increased charge recombination rates and reduced efficiency. The ability of a device to reliably detect radiation is a fundamental requirement for its practical industrial application.

Thin-film metal oxides (**TFMO**s) continue to attract considerable interest due to their versatility in sensing applications. Interest in modeling TFMOs has grown substantially over recent decades, driven by their relative simplicity and compatibility with available simulation tools. Nevertheless, most TFMO-based devices still exhibit low conversion efficiencies, and laboratory efforts to achieve optimal energy conversion continue despite advances in numerous physical and chemical fabrication methods for photovoltaic cells. This limitation can be attributed to several loss mechanisms inherent in absorber layer structures. Zinc oxide is widely used in optoelectronics owing to its excellent optical and electronic properties, and has established itself as a multifunctional material over the past five decades. ZnO is a wide-bandgap semiconductor with a bandgap of 3.36 – 3.41 eV, and is also regarded as an effective anti-reflection material suitable for optical detection and a broad range of optoelectronic applications [4]. Among heterojunction device architectures, the ZnO/Si thin-film heterostructure is one of the most extensively optimized configurations, demonstrating high photodetection efficiency. Key device parameters—

including absorber and electron transport layer (**ETL**) thickness, series resistance, shunt resistance, and operating temperature—can be evaluated together with corresponding characteristics such as carrier generation and recombination rates, capacitance–voltage (*C–V*) profiles, current density–voltage (*J–V*) curves, and quantum efficiency. These performance metrics are strongly influenced by crystallographic quality, surface morphology, and film density, making the choice of ZnO deposition technique critical for fabricating high-quality photosensitive structures [5]. Numerical simulations of low-cost ZnO/Si devices have previously been carried out using various tools, including AFORS-HET and PC1D [6], [7]. ZnO/Si photocells have also been modeled with Silvaco ATLAS, where bandgap profiles and electric field distributions at the Si/ZnO interface were examined [8]. The SCAPS-1D software enables numerical investigation of hetero- and multi-junction photovoltaic devices, supporting the extraction of photovoltaic parameters as well as non-standard measurements, including *C–V*, *G–V* (conductance–voltage), and *C–f* (capacitance–frequency) characteristics. It has also been applied to simulate ZnO/Si solar cells with interface defects [9]. Simulations were carried out using an iterative approach, solving the Poisson equation together with the continuity equations for electrons and holes [10], with photodetector parameters extracted under different spectral conditions. The resulting SCAPS-1D outputs can be benchmarked against those obtained from other simulation platforms [11], [12]. Among the most widely used simulation tools in recent years are COMSOL, Silvaco ATLAS, AMPS, wxAMPS, and SCAPS [13], [14].

Among the available simulation tools, SCAPS-1D is regarded as particularly accessible, offering a broad range of input and output parameters [15], [16]. Compared to other common platforms for photodetector analysis—such as TCAD, ANSYS Lumerical Charge, and COMSOL Multiphysics—SCAPS-1D occupies a distinct and well-established position in the field. Its open-source nature and intuitive interface have made it a de facto standard in photovoltaic research. The reliability of the software is supported by a strong agreement between simulation results and experimental data for both *p–n* and *n–i–p* device structures. SCAPS-1D is a numerical platform for analyzing and optimizing thin-film photovoltaic homo- and heterojunction structures through the self-consistent solution of Poisson's equation and the carrier continuity equations, enabling detailed analysis of multilayer heterojunctions by allowing independent variation of layer thickness, doping concentration, defect density, and bandgap [17], [18]. The simulator is built upon the numerical solution of the fundamental semiconductor equations—namely, the Poisson equation and the carrier continuity equations—ensuring accurate computation of *J–V* characteristics and quantum efficiency [19], [20]. This physically rigorous approach yields high fidelity in modeling the optoelectronic processes occurring within photodetector structures. The strong correspondence between simulated and experimental results establishes SCAPS-1D as a dependable tool for predictive device design, enabling the effective development of sensors for optical imaging, environmental monitoring, and operation across a broad spectral range.

The aim of this work is to investigate and analyze, by means of numerical simulation within the SCAPS-1D software environment, the parameters and characteristics of a ZnO/Si heterojunction photodetector. Particular attention is given to the influence of ZnO oxide layers grown on silicon substrates by pulsed laser deposition [21], [22] on the responsivity and specific detectivity of the device in the ultraviolet spectral region (300 nm).

Research Methodology and Subject of Investigation

This work employs a planar *p–n* heterojunction structure consisting of a *p*-type Si layer and an *n*-type ZnO thin film. Default device parameters are applied across configurations with different active layers. The photoelectric performance of the *n–p* ZnO/Si heterojunction was numerically evaluated using the fundamental equations governing electron–hole junctions, with simulations carried out in SCAPS-1D. Based on input parameters such as layer bandgap, thickness, and doping concentration, the software predicts key photovoltaic characteristics—including current–voltage curves, quantum efficiency, and energy band diagrams. The principal input parameters include dielectric permittivity, bandgap energy (E_g), electron affinity, carrier mobility, and doping concentrations (N_D, N_A). The generation rate is computed from the optical absorption profile under a specified illumination spectrum, while the recombination rate is determined self-consistently alongside the carrier transport equations. The platform also supports parametric optimization—for example, systematic variation of layer thickness or doping concentration—enabling quantitative assessment of their impact on power conversion efficiency (*PCE*) and fill factor (*FF*).

The thickness of the metal oxide film was varied in the range of 50 – 700 nm for the absorber layer, while the base layer (industrial-grade silicon wafers) had a fixed thickness of 250 μm. Planar configurations offer the advantage of low-temperature processing, which enables the fabrication of flexible devices without inducing substrate degradation. Furthermore, such configurations are compatible with tandem junction architectures incorporating a variety of semiconductor materials. The simulation results identify the optimal photodetection efficiency for a range of *p–n* parameter values of the ZnO/Si heterojunction.

ISSN 3083-6530 (Print)
ISSN 3083-6549 (Online)

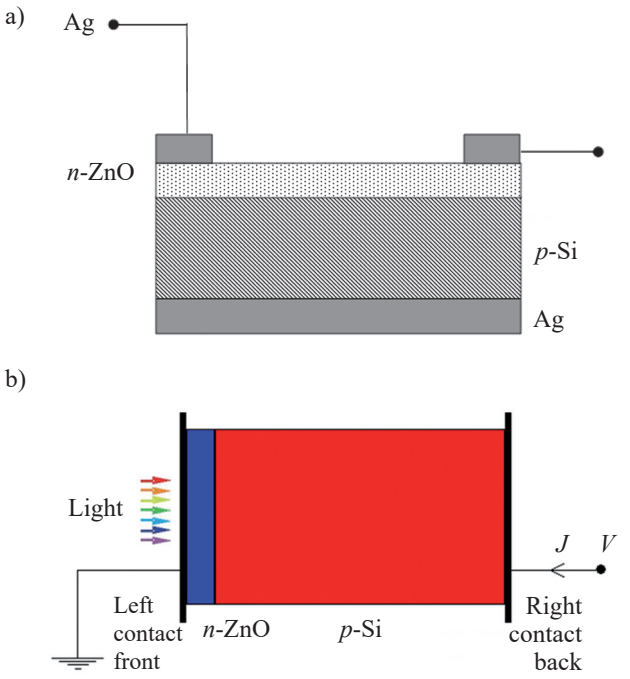

Fig. 1. Schematic representation of the *n*-ZnO/*p*-Si heterostructure (*a*) and device configuration used for numerical modeling in the SCAPS-1D simulation environment (*b*)

Since Si is a *p*-type semiconductor, an *n*-type electronically conductive metal oxide was incorporated as the photoabsorber within the heterojunction structure. ZnO thin film, owing to its favorable optoelectronic properties, serves as an *n*-type material functioning simultaneously as both the window and active layer. The relatively thick Si base provides strong optical absorption and forms a heterojunction that is well-matched to *n*-type thin-film overlayers. This configuration enables enhanced photocurrent generation upon interaction of ultraviolet photons with the active layer, allowing absorption of all photons with energies exceeding the bandgap of ZnO. Together, the *n*-type absorption layer and the *p*-type silicon layer constitute a conventional photovoltaic structure with a window–absorber *n*–*p* junction, as illustrated in **Fig. 1**. In a homojunction device, both regions are composed of the same semiconductor material, whereas in a heterojunction device they consist of two distinct materials.

The interface between the *p*- and *n*-type regions is regarded as the most critical component of any photovoltaic device. Within this region of the heterostructure, energetic photons absorbed in the space-charge depletion region drive the separation of electron-hole pairs, a process that plays a decisive role in determining overall device performance.

Numerical Simulation Using SCAPS-1D

Simulations were performed using SCAPS version 3.3.12, a software package widely adopted for modeling photovoltaic cells based on polycrystalline thin films, which also supports the simulation of step junctions. The principal photovoltaic parameters—open-circuit voltage (V_{OC}), short-circuit current density (J_{SC}), fill factor (*FF*), quantum efficiency (*QE*), and the band structure of the heterojunction—are key determinants of photodetector responsivity [23], [24]. Simulations were conducted under spectral illumination conditions, within which a variety of homo- and heterojunction architectures can be proposed and evaluated [25], [26].

The simulation framework is based on the self-consistent numerical solution of Poisson's equation and the semiconductor continuity equations. The continuity equations, solved within the junction interface region, govern charge carrier transport inside the device—accounting for electrostatic potential distribution, carrier drift and diffusion, and electron-hole recombination processes [27]. Poisson's equation is given as

$$\nabla^2\varphi = -\frac{q}{\varepsilon}(n - p + N_D - N_A), \quad (1)$$

where φ is the electrostatic potential;
ε is the dielectric permittivity;
q is the elementary charge;
N_A, N_D are the acceptor and donor densities, respectively;
p, n are the hole and electron concentrations, respectively.

The semiconductor carrier transport equations are given as

$$\nabla J_p = q(G - R); \quad (2)$$

$$\nabla J_n = q(R - G), \quad (3)$$

where J_p, J_n are the hole and electron current density, respectively;
G is denotes the optical generation rate;
R is the total recombination, including direct and indirect recombination.

All these parameters are a function of the interface coordinate (coordinate position x). Introducing the effective potentials V_n and V_p as characteristic quantities of the interface region, we obtain

$$V_n = V + \gamma\frac{\Delta G}{g}; \quad (4)$$

$$V_p = V - (1-\gamma)\frac{\Delta G}{g}. \quad (5)$$

The parameters ΔG and γ take into account changes in the band structure, such as the density of states of the band gap, and also take into account Fermi–Dirac statistics. Then the hole and electron current densities appearing in equations (2) and (3) are given by

$$J_p = -q\mu_p p \cdot \nabla V_p - kT\mu_p \cdot \nabla p; \quad (6)$$

$$J_n = -q\mu_n n \cdot \nabla V_n - kT\mu_n \cdot \nabla n, \quad (7)$$

where μ_n, μ_p are the electron and hole mobilities, respectively.

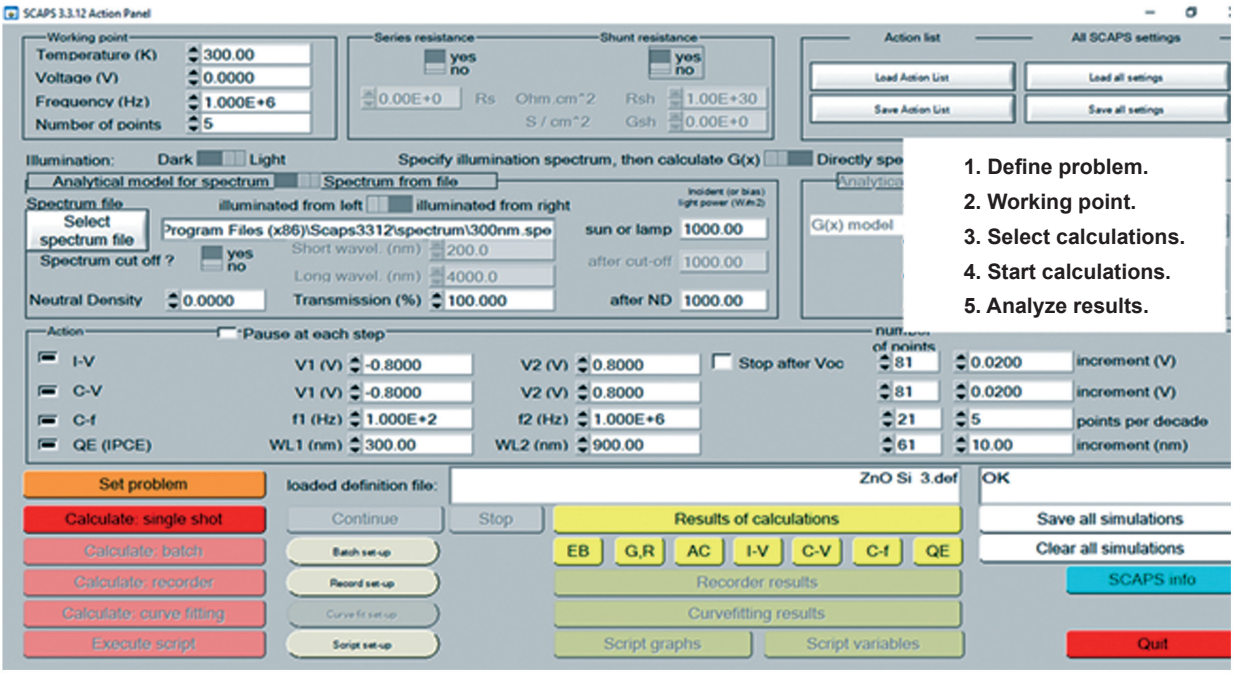

Fig. 2. SCAPS-1D simulation platform for modeling the optoelectronic properties of the *n*-ZnO/*p*-Si heterojunction

The software interfaces use all the variables listed in **Table 1** and are the device input parameters during the simulation.

All variables listed in Table 1 serve as device input parameters during simulation and are directly accessible through the software interface. The complete modeling procedure for characterizing a heterojunction is outlined in the flowchart presented in **Fig. 2**.

Table 1

Device parameters: ZnO layer and substrate p-Si [28]

Parameters	*n*-ZnO	*p*-Si
Relative permittivity, ε_r	9	11.9
Energy gap, E_g (eV)	3.3	1.12
Thickness, d (μm)	variable	250
Electronic affinity, χ (eV)	4.35	4.05
Effective density of states in the conduction band, N_C (cm^{-3})	$4.4 \cdot 10^{18}$	$2.8 \cdot 10^{19}$
Effective density of states in the valence band, N_V (cm^{-3})	$7.1 \cdot 10^{19}$	$1.04 \cdot 10^{18}$
Donor concentration, N_D (cm^{-3})	variable	—
Acceptor concentration, N_A (cm^{-3})	—	$7.0 \cdot 10^{15}$
Electron mobility, μ_n ($cm^2/V \cdot s$)	100	1500
Hole mobility, μ_p ($cm^2/V \cdot s$)	25	480
Electron thermal velocity, $V_{th.e}$ (cm/s)	10^7	10^7
Hole thermal velocity, $V_{th.h}$ (cm/s)	10^7	10^7
Temperature, T (K)	300	300

The key outputs generated by SCAPS-1D include:

• *J–V* curves, used for optimizing the power conversion efficiency;

• quantum efficiency describing photon-to-carrier conversion as a function of wavelength;

• energy band diagrams providing visualization of band alignment and Fermi-level (E_F) distribution;

• capacitance–voltage characteristics, enabling determination of carrier concentration and built-in potential.

In each simulation run, the primary variable (voltage V, frequency f, or current I) is swept across a specified range. The resulting outputs include computed parameters and characteristics—such as *J–V* and *C–V* curves, *C–f* spectra, generation rate profiles $Q(\lambda)$, energy band diagrams, carrier concentration distributions, and electron and hole current densities. All simulation results are exported in ASCII format and presented graphically for analysis and interpretation.

Results and Discussion

SCAPS-1D Simulation of the n–p ZnO/Si Heterojunction

This study examined the effect of ZnO layer thickness on the characteristics of the ZnO/Si heterojunction. The simulation incorporated a nickel-doped zinc oxide layer serving as an ultraviolet-absorbing medium. *J–V* curves were extracted from spectral measurements performed both in the dark and under illumination, reflecting realistic device operating conditions. The highest fill factor of 63.18% and power conversion efficiency of 7.71% were achieved for the nanostructured ZnO/Si heterojunction with an absorber layer thickness of 100 nm.

ISSN 3083-6530 (Print)
ISSN 3083-6549 (Online)

The input parameters used in the SCAPS-1D simulations were adopted from the literature and are based on the material properties of ZnO and Si summarized in Table 1.

The input parameters for the front and rear contacts were additionally optimized using SCAPS-1D.

Properties of the ZnO Absorber Layer

The absorption layer consists of an *n*-type zinc oxide semiconductor. ZnO exhibits an electron affinity of 4.5 eV and favorable carrier mobility characteristics. In addition, ZnO possesses distinctive optoelectronic properties, high mechanical strength, and a large refractive index, making it a highly suitable material for a broad range of applications, including photovoltaics. The density of states is governed by the strong hybridization between the constituent atomic orbitals. Among all orbital contributions, the O2p orbital electrons exert the dominant influence on the position of the Fermi level E_F. The electronic band structure and density of states represent energy spectra that describe the dependence of energy eigenvalues on wave vectors in the reciprocal (*k*-space) of a crystal lattice, encoding information about both intramolecular bond interactions and intermolecular forces.

The electron affinity of ZnO, acting as the electron transport material, ranges from 3.60 to 4.60 eV. By adjusting this parameter, the band offset at the interface with the absorber layer can be tuned, effectively shifting the energy band alignment. A schematic of the energy band diagram of the simulated *n*-ZnO/*p*-Si photovoltaic structure is presented in **Fig. 3**. In this configuration, the *n*-ZnO layer serves as the photoabsorber, while the *p*-Si layer functions as the primary charge transport medium.

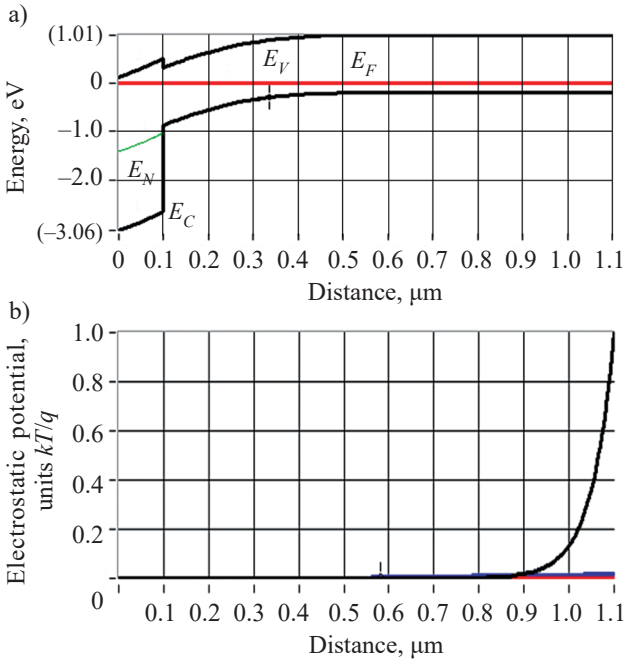

Fig. 3. Spatial distribution of energy bands (*a*) and electrostatic potential in ZnO/Si heterostructures (*b*)

Simulated Current-Voltage Characteristics of the ZnO/Si Heterojunction

Representative transport curves across the heterojunction interface. Representative transport curves across the ZnO/Si heterojunction interface were obtained under the following simulation conditions: illumination incident from the left contact, voltage bias applied at the right contact, and the left contact held at ground potential. Layer interfaces were defined accordingly. The simulation first computed the energy band structure, followed by extraction of the *J–V* and *C–V* characteristics. The simulated ZnO/Si thin-film heterojunction yielded a fill factor of $FF \approx 63.18\%$ and a power conversion efficiency of $\eta \approx 7.71\%$. **Fig. 4** presents the dark and illuminated current–voltage characteristics over a bias range of −0.8 V to +0.8 V, where the photocurrent consistently exceeded the dark current [29]. The photovoltaic parameters derived from the *J–V* curves are summarized in **Table 2**.

Careful analysis reveals the coexistence of several conduction mechanisms, giving rise to non-ideal diode

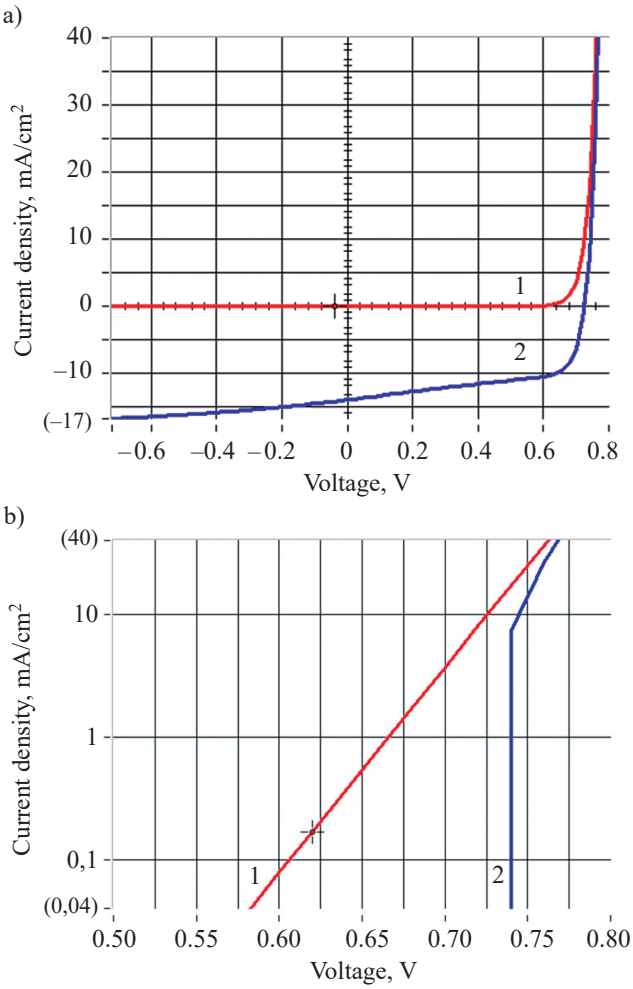

Fig. 4. Current–voltage characteristics of the ZnO/Si photodetector, presented on a linear scale (*a*) and a semi-logarithmic scale (*b*):

1 — dark; *2* — under UV illumination at λ = 300 nm

Table 2

Summary of input parameters for the back and front contacts employed in SCAPS-1D simulations of metal oxide-based heterojunction devices

Parameter	Back contact	Front contact
Thermionic emission/surface recombination velocity Holes (cm/s)	$1.00 \cdot 10^7$	$1.00 \cdot 10^7$
Thermionic emission/surface recombination velocity Electrons (cm/s)	$1.00 \cdot 10^7$	$1.00 \cdot 10^7$
Metal work function (eV)	5.021	—
Main carrier barrier height (eV) relative to E_f	0.221	0.4
Main carrier barrier height (eV) relative to E_v	0	0.227

behavior in distinct operating regions. The forward bias regime can be decomposed into three characteristic transport regimes: generation-recombination current, diffusion current, and an ohmic regime governed by series resistance [30]. At low forward bias, carrier transport is dominated by recombination via the Shockley–Read–Hall (**SRH**) mechanism, involving defect states and trap centers within the depletion region. At moderate forward bias, diffusion current becomes the primary transport mechanism, as injected minority carriers—holes in the n-type region and electrons in the *p*-type region—diffuse into the quasi-neutral regions, producing an exponential current–voltage dependence. In this regime, the *J–V* characteristic approaches ideal Shockley behavior with an ideality factor close to unity, indicative of transport limited by minority carrier concentration gradients. The built-in potential of the heterojunction facilitates the separation of photogenerated charge carriers. In the absence of an external bias, the resulting potential difference across the device constitutes the fundamental driving mechanism of the photovoltaic effect. The short-circuit current exhibits a linear dependence on incident optical power, while the open-circuit voltage scales logarithmically with decreasing power, consistent with the heterojunction equation under illumination.

The dark *J–V* characteristic displays a nonlinear increase in current with applied voltage, which becomes particularly pronounced at higher bias levels. Under illumination at a power density of 82.7 mW/cm^2, the *J–V* characteristic is recorded for both reverse and forward bias conditions, as shown in Fig. 4. The carrier concentration directly influences the shape of the *J–V* curves: as the doping concentration increases, the resistivity decreases and the current increases correspondingly.

The described device operates in a one-sided structure, but ZnO plays an active role as the main absorbing layer in the ultraviolet region. The internal electric field of the heterojunction enables rapid separation of photoexcited electrons and holes [31]. This behavior is attributed to the high quality of the films and the low defect density of the fabricated ZnO and Si nanostructures, consistent with the estimated optical band gaps of the components used [32].

The current measured at a given voltage under illumination exceeds that recorded in the dark, confirming that light absorption in the *n*-ZnO/*p*-Si heterojunction generates a photocurrent through the formation of electron–hole pairs (**Fig. 5**). The enhancement of the reverse current under illumination is attributed to the generation of additional charge carriers via light absorption. The difference between the illuminated and dark currents, $I_{ill} - I_{dark}$, is 13.9 mA. The properties of both front and rear contacts can be independently adjusted, and the interface defect density between adjacent layers can be specified as a simulation input. **Table 3** summarizes the key simulated photovoltaic parameters—open-circuit voltage V_{OC}, short-circuit current density J_{SC}, fill factor *FF*, and power conversion efficiency η—extracted under illumination. From the *J–V* curve of the ZnO/Si

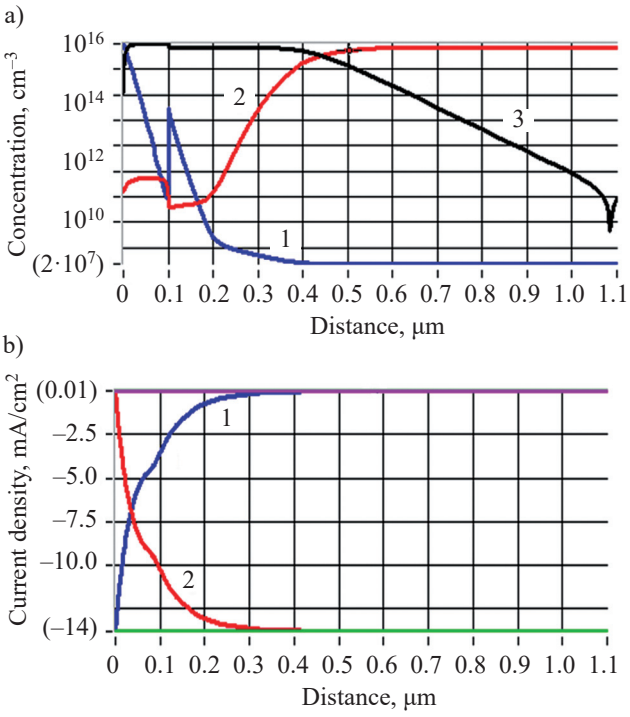

Fig. 5. Modeled carrier concentration (*a*) and current density (*b*) distributions of the ZnO/Si photodetector under UV illumination:

1 — electrons; *2* — holes; *3* — total concentration

Table 3

Simulated photoelectric parameters of the n-ZnO/p-Si photovoltaic heterojunction

V_{OC}, V	J_{SC}, mA/cm^2	*FF*, %	η, %
0.725	13.9	63.18	7.71

ISSN 3083-6530 (Print)
ISSN 3083-6549 (Online)

heterojunction photodetector, the short circuit current J_{SC} = 13.9 mA and the open circuit voltage V_{OC} = 0.725 V are obtained, consistent with the standard *J–V* response of a photovoltaic cell under illumination [33]. Variation of the electron affinity parameter affects the band alignment at the heterojunction interface and, if not correctly selected, results in a concurrent degradation of *FF*, J_{SC}, V_{OC}, and η.

Effect of ZnO layer thickness on structured heterojunction photovoltaic cells. In a typical *n–p* heterojunction, incident radiation passes through the absorber layer and partially through the conductive substrate. Incident photons are absorbed by the *n*-type semiconductor absorber layer, while unabsorbed photons are dissipated as heat. The absorber layer consists of a ZnO thin film, and the influence of doping concentration on device efficiency and *J–V* characteristics has been examined [34], [35]. Previous studies have demonstrated that ZnO is the most suitable *n*-type material for high-efficiency ZnO-based *p–n* heterojunction photovoltaic cells [36]. In the present study, the absorber layer thickness was varied in the range of 50 – 500 nm (**Fig. 6**). These values fall within the optimized thickness range; the absorber layer should be sufficiently thin to minimize series resistance within the photovoltaic device. As evident from the data shown in Fig. 6, the optimal ZnO layer thickness lies in the range of 50 – 100 nm. At this thickness, the heterostructure attains maximum photosensitivity in the ultraviolet spectral region.

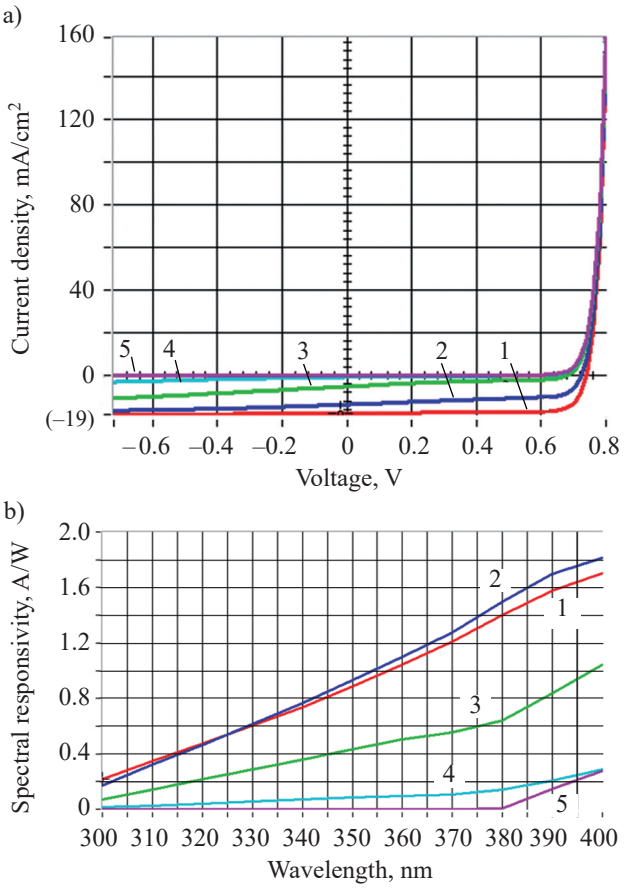

Fig. 6. Current-voltage characteristics (*a*) and spectral responsivity (*b*) of the *n*-ZnO/*p*-Si heterojunction at different ZnO absorber layer thicknesses (nm):

1 — 50; *2* — 100; *3* — 200; *4* — 300; *5* — 500

(donor concentration in ZnO $N_D = 10^{15}$ cm^{-3})

The optical absorption properties of each layer can be defined either through a built-in analytical model or by importing material property files from the program's internal library. Within the defect configuration panel, recombination is categorized into three distinct mechanisms: Auger recombination, radiative recombination (both representing band-to-band transitions) and SRH recombination, which proceeds via mid-gap trap states. In the present model, only SRH recombination is activated, defined by a single neutral defect level with uniform energy distribution and a defect density of $1 \cdot 10^{15}$ см$^{-3}$.

Therefore, the *n*-ZnO/*p*-Si heterostructure achieves maximum photosensitivity in the ultraviolet spectral region at an absorber layer thickness of approximately 50 – 100 nm.

Effect of absorber layer doping concentration on device performance. The doping concentration of the absorber layer has a significant influence on device performance and was varied in the range of $1 \cdot 10^{14}$ cm^{-3} to $1 \cdot 10^{18}$ cm^{-3} to examine its effect on the simulated characteristics.

A maximum power conversion efficiency of 7.71% is achieved following the optimization and verification of key simulation parameters. To further refine the properties of each active layer, the effects of absorber thickness and doping density on device performance (**Fig. 7**), efficiency, and carrier recombination behavior were systematically investigated. These results demonstrate that SCAPS-1D is capable of detecting variations in photovoltaic parameters and quantifying their impact on simulation output.

The donor concentration in a semiconductor can be controlled through intentional doping with extrinsic impurities or by modifying intrinsic defect populations. Zinc oxide, in particular, exhibits intrinsic *n*-type conductivity. The primary intrinsic donor-type defects in ZnO are oxygen vacancies and interstitial zinc atoms. The donor concentration can also be tuned by modifying the density of these intrinsic defects through post-deposition treatments such as thermal annealing or high-dose irradiation. As evident from Fig. 7, the optimal donor concentration in the ZnO layer for achieving high photocurrent responsivity lies in the range of $10^{14} – 10^{15}$ cm^{-3}.

The influence of trap defect density N_t on the heterostructure characteristics was also examined. Using SRH recombination model [37], a defect level was introduced with a mean energy of 0.58 eV within the bandgap and a neutral Gaussian energy distribution.

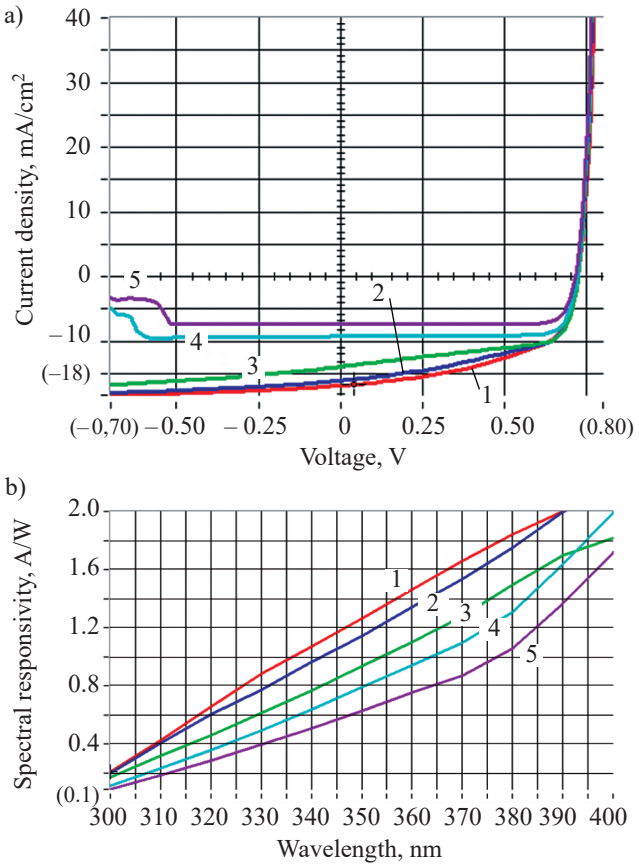

Fig. 7. Current-voltage characteristics (*a*) and spectral responsivity (*b*) of the *n*-ZnO/*p*-Si heterojunction at different donor concentrations in the ZnO layer (cm^{-3}):
1 — 10^{14}; *2* — 10^{15}; *3* — 10^{16}; *4* — 10^{17}; *5* — 10^{18}
(layer thickness 100 nm)

The SRH recombination rate is defined by equation

$$SRH = \frac{np - n_i^2}{\tau_p(n + n_i) + \tau_n(p + n_i)}, \quad (8)$$

where p, n denote the hole and electron concentrations;
τ_p, τ_n are the corresponding non equilibrium minority carrier lifetimes;
n_i is the intrinsic carrier concentration.

The model additionally computes the carrier diffusion length, as SRH recombination is one of the most prevalent recombination mechanisms in photodetector structures [38]. In this study, the trap defect density was set to $N_t = 1 \cdot 10^{15}$ cm^{-3}, which proved optimal for the given device configuration. The simulated device characteristics exhibit a systematic degradation with increasing defect density in the active absorber layer. The simulation framework also allows the defect density of the photoactive layer to be selectively disabled, enabling assessment of its individual contribution to overall device performance.

Graph of capacitance and conductivity of a heterostructure. The capacitive characteristics of the heterostructure—specifically the capacitance-voltage (*C–V*) and capacitance-frequency (*C–f*) profiles—were obtained by numerical simulation. The *C–V* characteristics were evaluated over a bias range of ±0.8 V at a frequency of 1 MHz.

The dependence of the junction capacitance for an abrupt heterojunction at zero bias is given in [39]:

$$C^2 = \frac{q\varepsilon_1\varepsilon_2 N_D N_A}{2(\varepsilon_1 N_D + \varepsilon_2 N_A)} \cdot \frac{1}{V_{bi} - V}, \quad (9)$$

where q is the elementary electron charge;
ε_1, N_D are the permittivity and donor carrier concentration of the ZnO layer, respectively;
ε_2, N_A are the permittivity and acceptor carrier concentration of the *p*-Si substrate, respectively.

The built-in potential V_{bi} is determined from the difference in energy levels on the band diagram (see Fig. 3, *a*). Its value at a donor concentration of $N_D = 10^{15}$ cm^{-3} in the absorbing layer ZnO is $V_{bi} = 2.8$ V and varies only slightly with changes in doping concentration. The values of N_D and N_A estimated for the *n*-ZnO/*p*-Si heterojunction are in good agreement with those used in the modeling.

Fig. 8 presents the simulated frequency dependence of the electrical parameters of the *n*-ZnO/*p*-Si photovoltaic cell under zero external bias. The frequency was swept from 50 Hz to 5 MHz. Fig. 8, *a* shows that the capacitance remains approximately constant with increasing frequency throughout the simulated range. Two distinct regions are identifiable in the *C–f* characteristics. At low frequencies, the capacitance is nearly constant and approaches the quasi-static (DC) limit. At high frequencies, a pronounced variation is observed, attributed to trapped carriers transitioning between occupied and unoccupied states near the Fermi level. When the AC signal frequency matches the characteristic time constant of these traps,

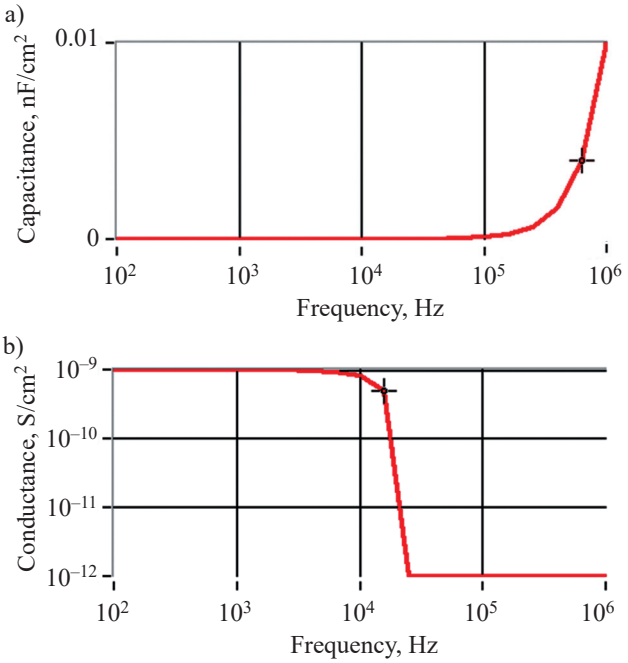

Fig. 8. Frequency dependences of the barrier capacitance (*a*) and specific admittance (*b*) of the *n*-ZnO/*p*-Si heterojunction

ISSN 3083-6530 (Print)
ISSN 3083-6549 (Online)

peak losses associated with interface trap levels are expected. For frequencies deviating slightly from this resonance condition, the interface density of states and the corresponding relaxation times can be estimated from the *C–f* plots.

The interface state density at the heterojunction interface was evaluated from the relationship between the surface charge density N_{ss} and the low-frequency capacitance C_{ss} [40]:

$$N_{ss} = \frac{C_{ss}}{q \cdot A}, \quad (10)$$

where A is the interface area.

The extracted interface state density is $N_{ss} = 3.63 \cdot 10^{-12}$ eV^{-1}·cm^{-2}.

In the MHz frequency range, significant changes in capacitance are observed. At sufficiently high frequencies, the device capacitance approaches the geometric capacitance, resulting in an apparent increase in the measured capacitance value when parasitic inductance effects are neglected.

The frequency dependence of heterostructures containing deep impurity levels arises from the charging and discharging dynamics of deep-level traps within the depletion region, which respond to the applied measurement frequency. When deep energy levels originate from a high concentration of intrinsic defects, the Schibli – Milnes model can be employed to describe the frequency dependence of the junction capacitance [41]. In the present work, this model was adopted to analyze the *C–f* characteristics of the device. Furthermore, it was confirmed that for short non equilibrium carrier lifetimes τ_{SRH} (corresponding to the short-diode limit), the barrier capacitance C_j is independent of the bulk layer thickness. Fig. 8, *b* shows the simulated conductance-frequency (*G–f*) characteristics of the ZnO/*p*-Si photovoltaic cell at different frequencies. The conductance decreases to values on the order of 10^{-12} S/cm^2 at frequencies above 10 kHz. In the high-frequency region, the device response is dominated by the series resistance and bulk properties of the semiconductor layers. The extracted values in this region enable quantification of contact and ohmic losses.

Noise Characteristics of the *n*-ZnO/*p*-Si Heterostructure

It is now widely accepted that current noise in semiconductors, metals, and electronic devices originates primarily from resistance fluctuations [42]. These fluctuations may arise from variations in carrier number, carrier mobility, or a combination of both. The 1/*f* noise spectrum emerges from the superposition of elementary stochastic events characterized by a broad distribution of time constants. In the McWhorter model, noise is attributed to the tunneling of carriers between the conducting channel and trap states in the oxide layer [43], [44]. Examples of such elementary events include changes in scattering cross-section due to carrier capture or emission by trap states, tunneling transitions between non-equivalent atomic configurations, and the motion of dislocations and grain boundaries [45]. Each elementary event is characterized by a specific time constant, and its contribution to the noise spectral density is described by a Lorentzian function. The relative contribution of each noise mechanism to the total noise spectral density depends on carrier concentration and the number of active carriers involved. Generation-recombination noise, arising from the capture and emission of charge carriers, represents one such mechanism. Consequently, Lorentzian-based noise relations are applicable only in specific limiting cases and are not valid when the dominant noise source is carrier mobility fluctuations.

In the case where the elementary event corresponds to carrier capture and emission throughgeneration-recombination noise at a localized energy level, the expression for the noise spectral density is given by [46]

$$S_I(f) = \frac{4I^2}{Vn_0^2} \cdot \frac{N_t \cdot \tau \cdot P(1-P)}{1 + (2\pi f\tau)^2}, \quad (11)$$

where N_t is the trap concentration;
V is the sample volume;
P is the energy level occupancy.

As can be seen, the noise spectral density is inversely proportional to the square of the free electron concentration n_0 ($\propto 1/n_0^2$). The noise spectral density in this model is also expressed in terms of N_t, the volumetric trap concentration given in units of cm^{-3}·eV^{-1}. The total noise spectral density depends on the thickness of the metal oxide active layer (**Fig. 9** and **Fig. 10**), as well as on the total number of charge carriers in the sample (**Fig. 11**).

Consider the practically important case of a semiconductor resistor uniformly doped with shallow impurities—specifically shallow donors (and acceptors) at concentration N_t. At a given temperature, the shallow level is fully ionized, and the equilibrium electron concentration satisfies $n_0 = N_t$. In addition, a relatively deep localized trap level is present at a concentration N_t. Under thermal equilibrium, the rates of carrier capture and emission are equal. When concentration fluctuations are governed by a single trap type, the resulting noise is of the generation-recombination type. However multiple trap levels with a corresponding distribution of characteristic time constants contribute collectively, 1/*f* noise arises, and the concentration dependence of the noise spectral density can deviate from the $1/n_0^2$ law.

For a simple two-level system, the standard theory of generation-recombination noise assumes the existence of a generation probability per unit time $g(N)$ and a recombination probability per unit time $r(N)$, describing transitions from the impurity level to the conduction band and the reverse process, respectively, within the framework of the detailed balance equation. In

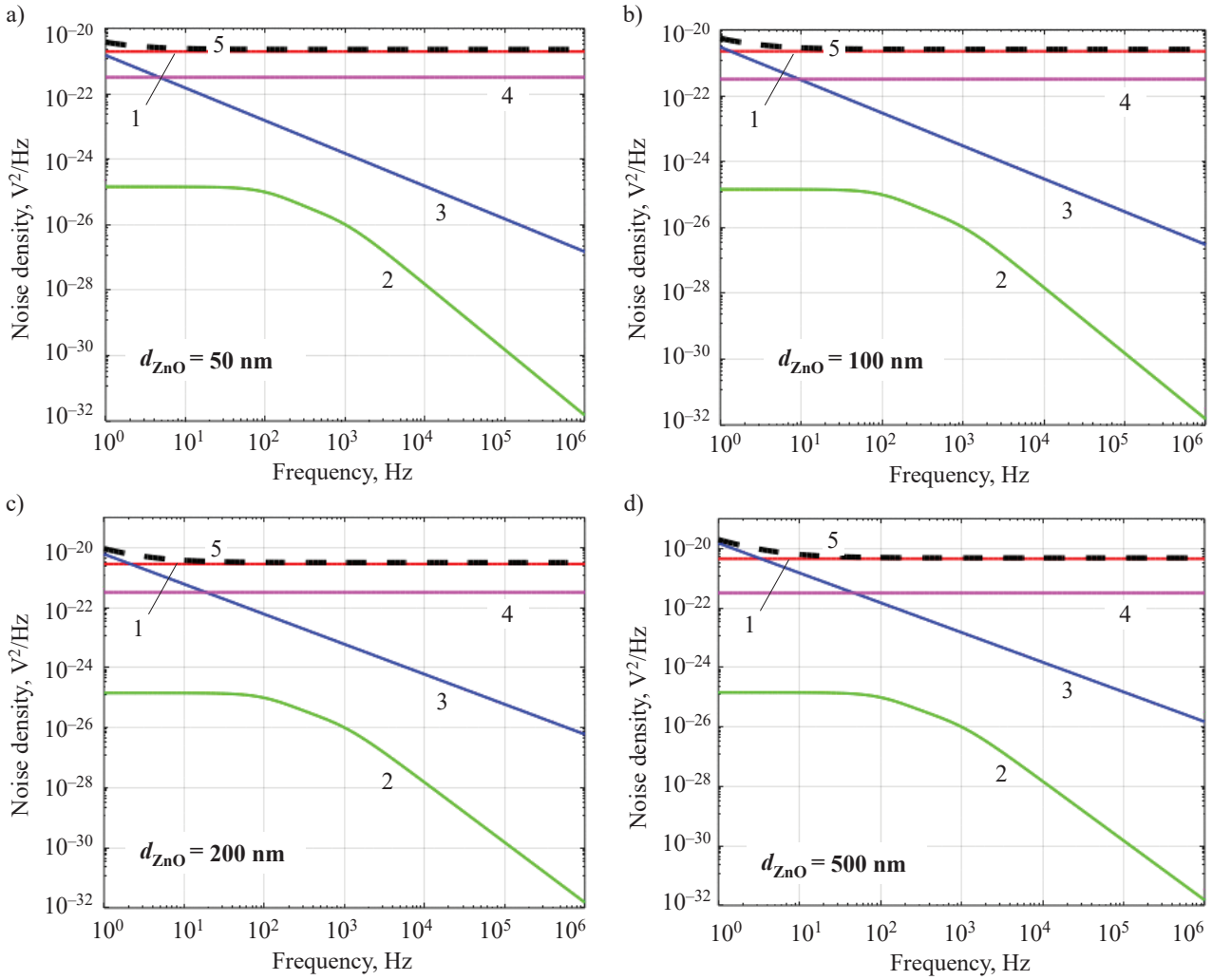

Fig. 9. Noise spectral characteristics of the *n*-ZnO/*p*-Si heterostructure for different ZnO absorber layer thicknesses d_{ZnO}: *1* — thermal noise; *2* — GR noise; *3* — 1/*f* noise; *4* — shot noise; *5* — total noise

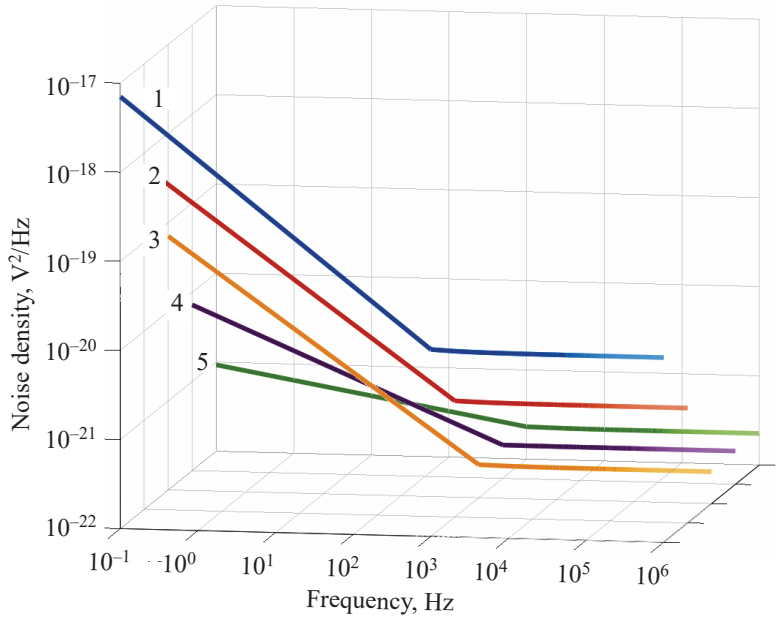

Fig. 10. Noise spectral characteristics of the *n*-ZnO/*p*-Si heterostructure with different concentrations of electron traps in the ZnO layer (cm^{-3}): *1* — 10^{14}; *2* — 10^{15}; *3* — 10^{16}; *4* — 10^{17}; *5* — 10^{18} (layer thickness 300 nm)

ISSN 3083-6530 (Print)
ISSN 3083-6549 (Online)

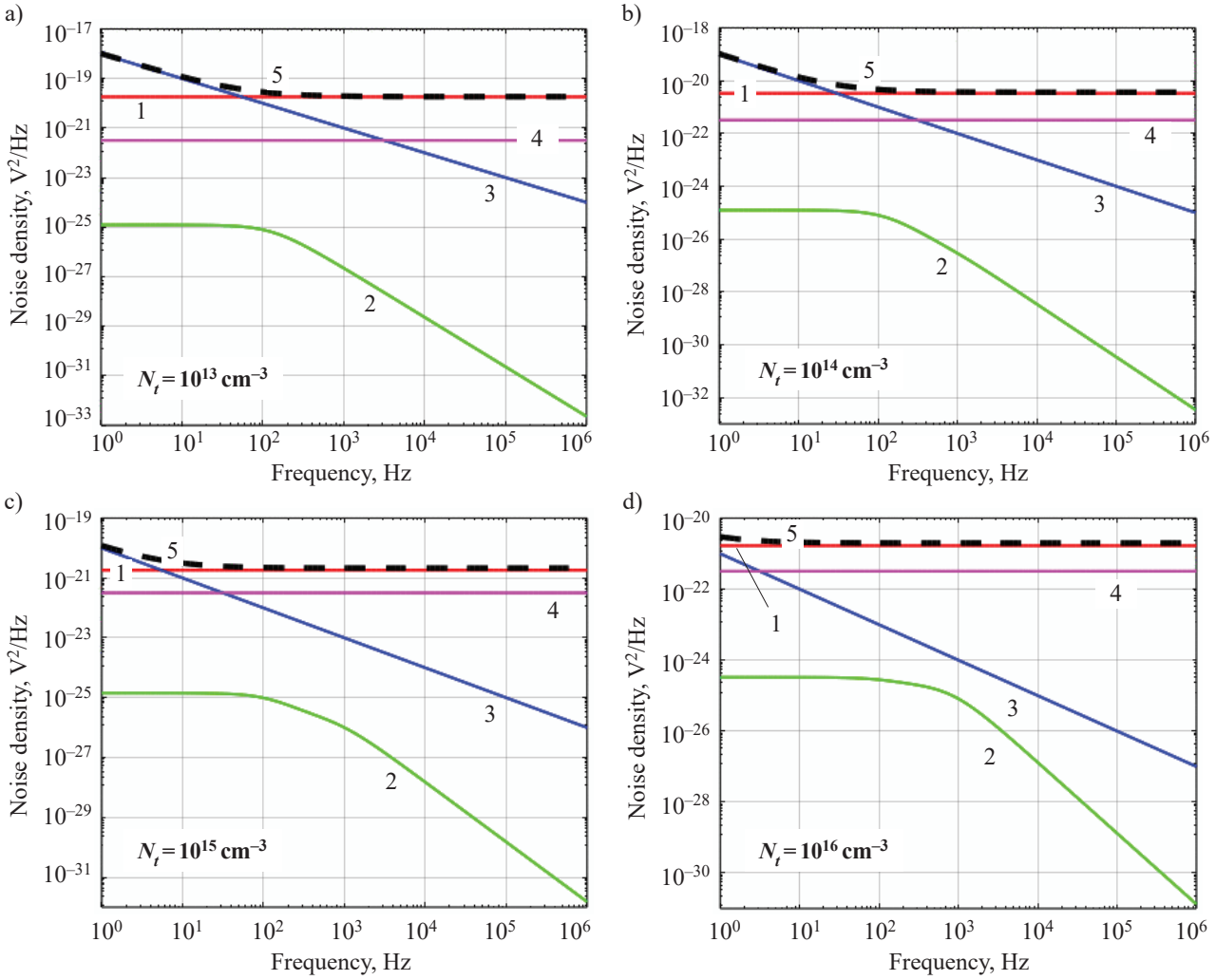

Fig. 11. Noise spectral characteristics of the *n*-ZnO/*p*-Si heterostructure for different concentrations of electron traps in the ZnO layer N_t:
1 — thermal noise; *2* — GR noise; *3* — 1/*f* noise; *4* — shot noise; *5* — total noise
(layer thickness 300 nm)

```
% Model parameters
k = 1.38e-23;      % Boltzmann's constant(J/K)
T = 300;           % Temperature (K)
R1 = 1;            % Resistance (Ohm)
q = 1.6e-19;       % Electron charge (C)
tau1 = 2e-4;       % Carrier lifetime (s)
nt1 = 1e13;        % ZnO trap concentration (1/cm^3)
p = 1e15;          % Si hole concentration (1/cm^3)
tauSi= 1.2e-3;     % Carrier lifetime (s)
RSi=0.1;
I = 1e-3;          % Current (A)
alpha1 = 1e-12; % Noise figure for 1/f
f = logspace(0, 6, 100); % Frequencies from 1 Hz to 1 MHz
% Thermal noise (Johnson-Nyquist noise)
S_V_thermal1 = 4 * k * T * (R1+RSi) * ones(size(f));
% GR-noise
S_I_GR1 = (4 * q^2 *((tau1 * nt1)./ (1 + (2 * pi * f * tau1).^2)+(tauSi * p) ./ (1 + (2 * pi * f * tauSi).^2)));
% Noise 1/f
S_I_flicker1 = alpha1 * I^2 ./ f;
% Schottky noise
S_I_shot1 = 2 * q * I * ones(size(f));
% Total noise spectral density
```

Fig. 12. Octave software interface for simulating the noise power spectral density of the *n*-ZnO/*p*-Si heterostructure

general, g is a monotonically decreasing function of N, while r is a monotonically increasing function of N; the exact forms of these functions are determined by the physical process under consideration. Under steady-state conditions, the balance between generation and recombination is established at $g_0 \approx g(N_t)$ and $r_0 \approx r(N_t)$. The values of g and r can be obtained by physically modeling the respective generation and recombination processes. Based on these calculations, the total noise spectral density of the heterostructure can be estimated numerically, for example using the Octave software environment (**Fig. 12**).

Quantum Efficiency Characteristics

The *QE* of a photovoltaic cell is influenced by a range of factors, including material properties, absorber layer thickness, and fabrication quality, as illustrated in **Fig. 13**.

The photoresponse of the device is also strongly dependent on the polarization state of the incident illumination. The photodetector based on the optimized heterojunction exhibits a broad spectral photoresponse spanning the ultraviolet region. The results demonstrate

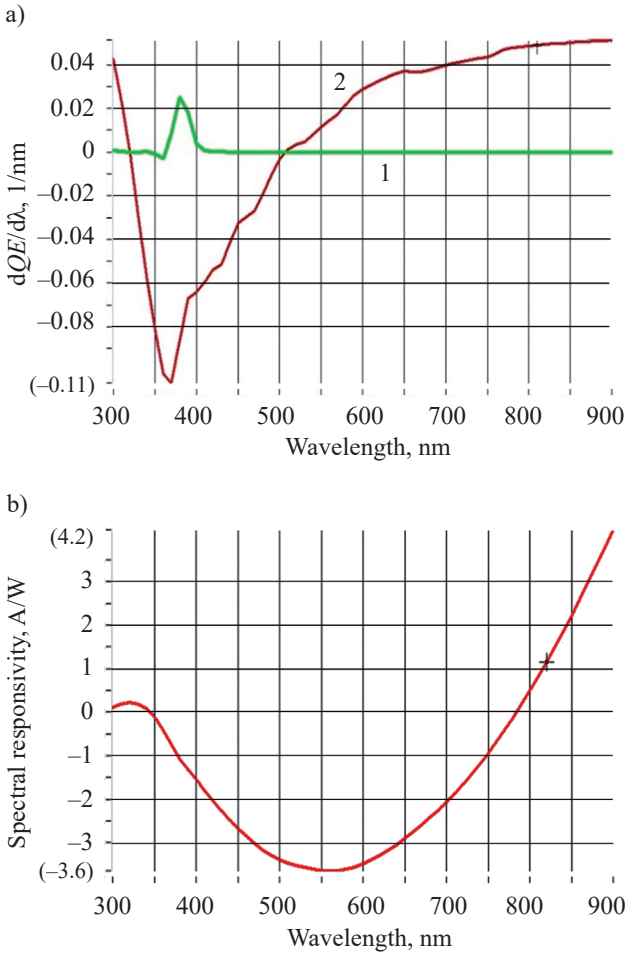

Fig. 13. Spectral dependencies of the derivative of the reduced quantum efficiency dQE/dλ in dark (*1*) and illuminated (*2*) conditions (*a*), and responsivity (*b*) of the ZnO/Si heterostructure

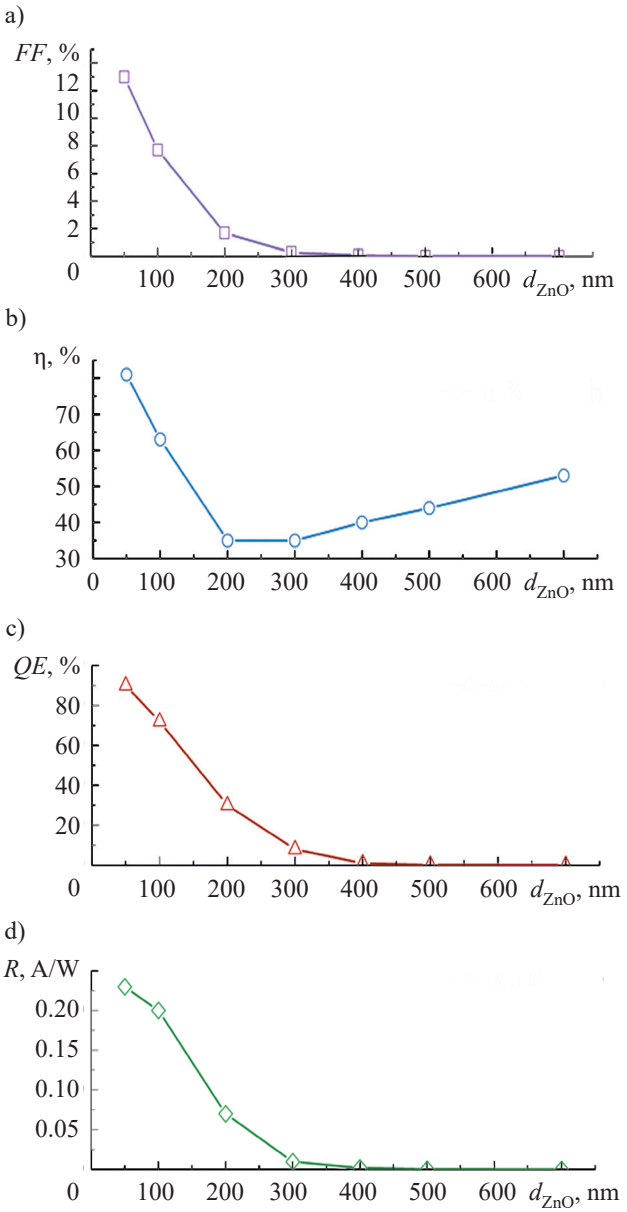

Fig. 14. Dependence of the fill factor *FF* (*a*), efficiency η (*b*), quantum efficiency *QE* (*c*), and responsivity *R* (*d*) of the *n*-ZnO/*p*-Si heterostructure on the thickness d_{ZnO} of the ZnO absorbing layer

well-pronounced photodetection performance under ultraviolet irradiation, while the photosensitivity decreases appreciably in the visible spectral region. The high responsivity and on/off photocurrent ratio of the ZnO/Si device are attributed to enhanced charge carrier separation, facilitated by the interfacial coupling effect between the ZnO thin film and the Si substrate.

Responsivity *R* and specific detectivity *D** are the key figures of merit for evaluating photodetector performance and assessing detection sensitivity. Assuming that shot noise originating from the dark current is the dominant contribution to the total noise, *R* and *D** can be expressed as [47]:

ISSN 3083-6530 (Print)
ISSN 3083-6549 (Online)

$$R = \frac{I_{\text{light}}}{W_{\text{in}} A}\ ;\ D^* = \frac{R\sqrt{A}}{\sqrt{2qI_{\text{dark}}}}, \qquad (12)$$

where W_{in} is the incident light intensity;
A is the effective area of the device;
q is the elementary charge ($q = 1.60 \cdot 10^{-19}$ C);
$2q \cdot I_{\text{dark}}$ is the shot noise current density.

Under ultraviolet illumination, the achieved responsivity of the photodetector is 0.23 A/W, and the specific detectivity is $1.1 \cdot 10^{10}$ Jones ($\text{cm} \cdot \text{Hz}^{-1/2} \cdot \text{W}^{-1}$), as shown in Fig. 13, *b*. The photovoltaic characteristics of the *n*-ZnO/*p*-Si heterostructure as a function of ZnO absorber layer thickness are presented in **Fig. 14**.

Conclusions

In this work, an *n*-ZnO/*p*-Si photodetector was numerically simulated and optimized using software SCAPS-1D. The simulated broadband ZnO/Si heterojunction photodetector exhibited a nonlinear increase in dark current as a function of applied voltage, consistent with the rectifying behavior of a *p–n* junction. The optimized heterojunction photodetector demonstrates a well-pronounced photoresponse across the spectral range of 200–400 nm. Under illumination, the optimal short-circuit current density reaches $J_{SC} = 13.9$ mA/cm^2, and the open-circuit voltage is $V_{OC} \approx 0.725$ V.

The simulation methodology for characterizing heterostructures is consistent with established standards. It enables the systematic selection of absorber layer thickness, electron affinity, and other electrophysical parameters for each constituent layer. Variation of the doping concentration in the absorber layer within SCAPS-1D yields a range of photovoltaic responses and responsivity values. Following optimization, the photosensitivity of the device is governed by the interplay between free carrier concentration and trap density. The improvement in the external quantum efficiency profile is primarily attributed to absorber layer optimization and, additionally, to the applied reverse bias voltage. The applied bias further enhances quantum efficiency by promoting charge carrier injection driven by photon absorption, as well as by the photon multiplication effect. At a wavelength of 300 nm, the optimized fill factor reaches 63.18%.

In summary, a self-powered photodetector based on the *n*-ZnO/*p*-Si heterostructure was numerically investigated and optimized using SCAPS-1D. The responsivity and specific detectivity of the simulated device are 0.23 A/W and $1.1 \cdot 10^{10}$ Jones, respectively. The simulation results highlight the potential of *n*-ZnO/*p*-Si-based optoelectronic devices and indicate a promising direction for further development. Further research should be directed toward the practical implementation and experimental verification of the proposed photodetector architecture.

REFERENCES

[1] M. Ta, N. Xue, A. Muhammad, et al., "Recent Progress in Photodetectors: From Materials to Structures and Applications," *Micromachines*, vol. 15, no. 10, p. 1249, pp. 1–28, 2024, doi: 10.3390/mi15101249.

[2] J. Qin, Z. Yan, and M. Huo, "Design of low-noise photodetector with a bandwidth of 130 MHz based on transimpedance amplification circuit," *Chinese Optics Letters*, vol. 14, no. 12, p. 122701, pp. 1–5, 2016, doi: 10.3788/COL201614.122701.

[3] S. Vaishnavi and G. Seetharaman, "Computational modelling and photovoltaic performance evaluation of various ETL/HTL engineered MASnI3 planar perovskite solar cell architectures using SCAPS-1D," *Energy Conversion and Management*, vol. 332, p. 119747, pp. 1–22, 2025, doi: 10.1016/j.enconman.2025.119747.

[4] D. K. Sharma, S. Shukla, K. K. Sharma, and V. Kumar, "A review on ZnO: Fundamental properties and applications," *Materials Today: Proceedings*, vol. 49, pt. 8, pp. 3028–3035, 2022, doi: 10.1016/j.matpr.2020.10.238.

[5] F. T. Z. Toma, M. S. Rahman, and K. H. Maria, "A review of recent advances in ZnO nanostructured thin films by various deposition techniques," *Discover Materials*, vol. 5, art. no. 60, pp. 1–31, 2025, doi: 10.1007/s43939-025-00201-1.

[6] B. Hussain, A. Aslam, T. M. Khan, et al., "Electron Affinity and Bandgap Optimization of Zinc Oxide for Improved Performance of ZnO/Si Heterojunction Solar Cell Using PC1D Simulations," *Electronics*, vol. 8, no. 2, p. 238, pp. 1–8, 2019, doi: 10.3390/electronics8020238.

[7] L. Chen, X. Chen, and Y. Liu, "Research on ZnO/Si heterojunction solar cells," *Journal of Semiconductors*, vol. 38, no. 5, p. 054005, pp. 1–11, 2017, doi: 10.1088/1674-4926/38/5/054005.

[8] H. Helal, M. B. Arbia, H. Pakdel, et al., "Enhanced NO2 Detection in ZnO-Based FET Sensor: Charge Carrier Confinement in a Quantum Well for Superior Sensitivity and Selectivity," *Chemosensors*, vol. 13, no. 10, p. 358, pp. 1–22, 2025, doi: 10.3390/chemosensors13100358.

[9] R. Szymon, E. Zielony, A. Lysak, and M. A. Pietrzyk, "Influence of the type of interlayer on current transport mechanisms and defects in n-ZnO/ZnCdO/p-Si and n-ZnCdO/ZnO/p-Si heterojunctions grown by molecular beam epitaxy," *Journal of Alloys and Compounds*, vol. 951, p. 169859, pp. 1–10, 2023, doi: 10.1016/j.jallcom.2023.169859.

[11] M. A. Salih, M. A. Mustafa, and B. A. A. Yousef, "Developing Lead-Free Perovskite-Based Solar Cells with Planar Structure in Confined Mode Arrangement Using SCAPS-1D," *Sustainability*, vol. 15, no. 2, art. 1607, pp. 1–18, 2023, doi: 10.3390/su15021607.

[12] H. Yao and L. Liu, "Design and Optimize the Performance of Self-Powered Photodetector Based on PbS/TiS3 Heterostructure by SCAPS-1D," *Nanomaterials*, vol. 12, art. 325, pp. 1–11, 2022, doi: 10.3390/nano12030325.

[13] G. C. EnSebe, K. Ukoba, and T.-C. Jen, "Numerical modeling of effect of annealing on nanostructured CuO/TiO2 pn heterojunction solar cells using SCAP," *AIMS Energy*, vol. 7, no. 4, pp. 527–538, 2019, doi: 10.3934/energy.2019.4.527.

[14] A. A. Goje, N. A. Ludin, M. A. M. Teridi, et al., "Design and Simulation of Lead-free Flexible Perovskite Solar cell Using SCAPS-1D," *IOP Conf. Series: Materials Science and Engineering*, vol. 1278, art. 012004, pp. 1–13, 2023, doi: 10.1088/1757-899X/1278/1/012004.

[15] E. L. Meyer, S. Jakalase, A. Nqombolo, et al., "The Numerical Simulation of a Non-Fullerene Thin-Film Organic Solar Cell with Cu_2FeSnS_4 (CFTS) Kesterite as a Hole Transport Layer Using SCAPS-1D," *Coatings*, vol. 15, no. 3, p. 266, pp. 1–21, 2025, doi: 10.3390/coatings15030266.

[16] A. Krishnan and T. D. Subash, "Simulation of NiOx Based Solar Cells Using SCAPS Software," *NanoWorld Journal*, vol. 9, no. S5, pp. S143–S148, 2023, doi: 10.17756/nwj.2023-s5-028.

[17] S. N. Shiddique, M. I. R. Ebon, M. A. H. Pappu, et al., "Design and simulation of a high performance Ag_3CuS_2 jalpaite-based photodetector," *Heliyon*, vol. 10, no. 11, e32247, pp. 1–15, 2024, doi: 10.1016/j.heliyon.2024.e32247.

[18] A. S. Alali, M. Oduncuoglu, H. Al-Dmour, and A. S. A. Ahmed, "Optimization of organic photodetectors using SCAPS-1D simulation: enhancing performance of PBDB-T-2F based devices through layer configuration and doping adjustments," *East European Journal of Physics*, vol. 1, pp. 151–159, 2025, doi: 10.26565/2312-4334-2025-1-14.

[19] A. Maoucha, F. Djeffal, T. Berghout, and H. Ferhati, "Photoresponsivity Enhancement of SnS-Based Devices Using Machine Learning and SCAPS Simulations," *Engineering Proceedings*, vol. 58, no. 1, N128, pp. 1–6, 2023, doi: 10.3390/ecsa-10-16014.

[20] I. Paul, A. I. Shimul, B. C. Biswas, et al., "Exploring optoelectronic and photovoltaic properties of Be3MF3 (M=P, As, Sb) perovskites via machine learning and numerical simulation," *Scientific Reports*, vol. 16, art. 3799, pp. 1–27, 2026, doi: 10.1038/s41598-025-34000-8.

[21] I. Virt, R. Gamernyk, P. Potera, et al., "Transient Photoconduction and Relaxation Photocurrent of ZnO Thin Films Produced by Pulsed Laser Deposition," *ECS Journal of Solid State Science and Technology*, vol. 11, no. 6, p. 063013, pp. 1–6, 2022, doi: 10.1149/2162-8777/ac765f.

[22] I. Virt, P. Potera, G. Gamernyk, and B. Cieniek, "Structural and optical properties of Ni-doped ZnO thin films as TCO material, fabricated by pulsed laser deposition method," *Optical Materials*, vol. 154, art. 115643, pp. 1–7, 2024, doi: 10.1016/j.optmat.2024.115643.

[23] A. D. Rana, I. D. Pharne, and K. Bhargava, "Numerical simulation of highly efficient double perovskite solar cell using SCAPS-1D," *Materials Today: Proceedings*, vol. 73, pt. 4, pp. 584–589, 2023, doi: 10.1016/j.matpr.2022.11.110.

[24] G. M. Mustafa, B. Younas, M. Falk, et al., "Modeling and numerical analysis of FTO/TiO2/Cs2BiAgI6/CBTS/Au solar cells for enhanced photovoltaic performance," *Inorganic Chemistry Communications*, vol. 175, no. 5, p. 114146, pp. 1–13, 2025, doi: 10.1016/j.inoche.2025.114146.

[25] T. A. Chowdhury, "SCAPS modeling and performance analysis of AZO/SnS2/CZTS solar cells," *Optics Continuum*, vol. 3, no. 8/15, pp. 1341–1368, 2024, doi: 10.1364/OPTCON.527415.

[26] A. Javed, M. F. Nasir, S. Azam, and M. A. Amin, "Numerical simulation for a suitable electron transport layer of a lead-free $CuInSe_2$ based perovskite solar cell and PV module," *International Journal of Electrochemical Science*, vol. 20, no. 1, p. 100893, pp. 1–13, 2025, doi: 10.1016/j.ijoes.2024.100893.

[27] T. Hidouri, S. Rabhi, H. Bencherif, and R. Fornari, "Design of CsSnBr3/Ga2O3 Hybrid Photodetectors for High UV Selectivity and Bifacial Usage," *Advanced Theory and Simulations*, vol. 8, p. e01163, pp. 1–11, 2025, doi: 10.1002/adts.202501163.

[28] İ. Kanmaz, "Simulation of CdS/p-Si/p+-Si and ZnO/CdS/p-Si/p+-Si heterojunction solar cells," *Results in Optics*, vol. 10, p. 100353, pp. 1–9, 2023, doi: 10.1016/j.rio.2023.100353.

[29] A. Houimi, S. Yiğit Gezgin, Y. Gündoğdu, and H. Ş. Kiliç, "I-V Characteristics Calculation Using SCAPS-1D," *Selcuk University Journal of Social and Technical Researches*, vol. 19, pp. 1–6, 2021.

[30] M. Khaouani, A. Sessa, S. De Stefano, et al., "Experiment and simulation in silicon PN-junction photodetectors: Insights into electrical and optical transport," *Physica B: Condensed Matter*, vol. 730, p. 418479, pp. 1–10, 2026, doi: 10.1016/j.physb.2026.418479.

[31] X. Chu, S. Liu, B.-B. Luan, et al., "Crystal-Facet-Controlled Internal Electric Field in MOF/COF Heterojunction Towards Efficient Photocatalytic Overall Water Splitting," *Angewandte Chemie International Edition*, vol. 64, p. e202422940, pp. 1–9, 2025, doi: 10.1002/anie.202422940.

[32] N. N. Malpure, S. R. Patil, J. V. Sali, et al., "Influence of Multilayer Architecture on the Structural, Optical, and Photoluminescence Properties of ZnO Thin Films," *Photonics*, vol. 12, no. 12, p. 1219, pp. 1–17, 2025, doi: 10.3390/photonics12121219.

[33] G. D. Obikoya, A. Soman, U. K. Das, and S. S. Hegedus, "Investigation into fill factor and open-circuit voltage degradations in silicon heterojunction solar cells under accelerated life testing at elevated temperatures," *Solar Energy Materials and Solar Cells*, vol. 263, p. 112586, pp. 1–28, 2023, doi: 10.1016/j.solmat.2023.112586.

[34] L. Chen, X. Chen, Y. Liu, et al., "Research on ZnO/Si heterojunction solar cells," *Journal of Semiconductors*, vol. 38, no. 5, art. 054005, pp. 1–11, 2017, doi: 10.1088/1674-4926/38/5/054005.

[35] O. A. Fahad, B. K. Al Rawi, A. Ramizy, and E. Y. Salih, "High-performance ZnO/CdTe/Ge/Si heterojunction photodetector for short/mid-wavelength detection," *Sensors and Actuators A: Physical*, vol. 383, art. 116198, pp. 1–8, 2025, doi: 10.1016/j.sna.2025.116198.

[36] A. D. Pogrebnyak, N. Jamil, and A. K. M. Muhammed, "Simulation Study of n-ZnO/p-Si Heterojunction Solar Cell," *Nanosystems, Nanomaterials, Nanotechnologies*, vol. 9, no. 4, pp. 819–830, 2011.

[37] H. Helal, M. B. Arbia, H. Pakdel, et al., "Enhanced NO_2 Detection in ZnO-Based FET Sensor: Charge Carrier Confinement in a Quantum Well for Superior Sensitivity and Selectivity," *Chemosensors*, vol. 13, no. 10, p. 358, pp. 1–22, 2025, doi: 10.3390/chemosensors13100358.

[38] E. L. Meyer, S. Jakalase, A. Nqombolo, et al., "The Numerical Simulation of a Non-Fullerene Thin-Film Organic Solar Cell with Cu2FeSnS4 (CFTS) Kesterite as a Hole Transport Layer Using SCAPS-1D," *Coatings*, vol. 15, no. 3, p. 266, pp. 1–21, 2025, doi: 10.3390/coatings15030266.

[39] M. Nasr, I. M. El Radaf, and A. M. Mansour, "Current transport and capacitance–voltage characteristics of an n-PbTe/p-GaP heterojunction prepared using the electron beam deposition technique," *Journal of Physics and Chemistry of Solids*, vol. 115, pp. 283–288, 2018, doi: 10.1016/j.jpcs.2017.12.029.

[40] A. O. Tezcan, A. B. Çavdar, S. Eymur, and N. Tuğluoğlu, "Frequency-dependent interface states and diode parameters of Au/n-Si Schottky diode with BOD-Z-EN interfacial layer in dark and under illumination," *Physica B: Condensed Matter*, vol. 710, p. 417273, pp. 1–8, 2025, doi: 10.1016/j.physb.2025.417273.

[41] Y. Kang, Y. Xu, D. Zhao, and J. Fang, "Frequency dependence of junction capacitance of GaN p–i–n UV detectors," *Solid-State Electronics*, vol. 49, no. 7, pp. 1135–1139, 2005, doi: 10.1016/j.sse.2005.05.001.

[42] F. N. Hooge, "On the additivity of generation–recombination spectra. Part 1: Conduction band with two centres," *Physica B: Condensed Matter*, vol. 311, no. 3–4, pp. 238–249, 2002, doi: 10.1016/S0921-4526(01)01027-4.

[43] F. N. Hooge, "On the additivity of generation–recombination spectra. Part 2: 1/f noise," *Physica B: Condensed Matter*, vol. 336, no. 3–4, pp. 236–251, 2003, doi: 10.1016/S0921-4526(03)00164-9.

[44] L. K. J. Vandamme and F. N. Hooge, "On the additivity of generation–recombination spectra. Part 3: The McWhorter model for 1/f noise in MOSFETs," *Physica B: Condensed Matter*, vol. 357, no. 3–4, pp. 507–524, 2005, doi: 10.1016/j.physb.2004.09.106.

[45] D. Kim, J.-W. Lee, J. Lim, et al., "Highly stable two-level current fluctuation in complex oxide heterostructures," *Nature Communications*, vol. 16, no. 1, art. 5459, pp. 1–10, 2025, doi: 10.1038/s41467-025-60672-x.

[46] S. A. Vitusevich, S. V. Danylyuk, A. M. Kurakinet, et al., "Origin of noise in heterostructures in the range of 10–100 MHz," *Journal of Applied Physics*, vol. 99, art. 073706, pp. 1–6, 2006, doi: 10.1063/1.2188048.

[47] F. Wang, T. Zhang, R. Xie, et al., "How to characterize figures of merit of two-dimensional photodetectors," *Nature Communications*, vol. 14, art. 2224, pp. 1–9, 2023, doi: 10.1038/s41467-023-37635-1.

Received 31 March 2026
Accepted 19 June 2026

ISSN 3083-6530 (Print)
ISSN 3083-6549 (Online)

DOI: 10.15222/TKEA2026.1.17
УДК 621.382.592

Ігор ВІРТ, Іван ПАДАЛКА

Україна, Дрогобицький державний педагогічний університет
імені Івана Франка

МОДЕЛЮВАННЯ ФОТОДІОДНОЇ СТРУКТУРИ НА ОСНОВІ ГЕТЕРОПЕРЕХОДУ ZnO/SI

У роботі чисельно досліджено та проаналізовано за допомогою програмного забезпечення Solar Cell Capacitance Simulator in One-Dimension (SCAPS-1D) фотодетектор з власним живленням, який використовує об'ємний n–p-гетероперехід n-ZnO/p-Si. SCAPS-1D — це числова платформа для аналізу та оптимізації тонкоплівкових фотоелектричних гомо- та гетероперехідних структур за допомогою самоузгодженого розв'язання рівняння Пуассона та рівнянь неперервності носіїв заряду, що дозволяє проводити детальний аналіз багатошарових гетеропереходів, дозволяючи змінювати товщину шару, концентрацію легування, щільність дефектів та ширину забороненої зони. Програмне забезпечення побудовано на числовому розв'язанні фундаментальних напівпровідникових рівнянь, а саме рівняння Пуассона та рівнянь неперервності носіїв заряду, що забезпечує точне обчислення J–V характеристик та квантової ефективності.

Досліджено енергетичні зони, залежність густини струму від напруги (J–V), спектральні характеристики фоточутливості та детектуючу здатність в ультрафіолетовому діапазоні. Використовувалися різні параметри для опису електронного транспорту у плівці ZnO. Оптимізацією підібрано товщину шарів ZnO та Si, які були визначені на рівні 100 та 700 нм відповідно. Концентрація неглибокого донора шару ZnO змінювалась у межах від 10^{14} до 10^{18} $см^{-3}$. Моделювання засвідчило, що фотодетектор на основі гетеропереходу з оптимальними параметрами характеризується значним фотовідгуком при опромінюванні ультрафіолетом із довжиною хвилі 300 нм. В умовах освітлення оптимальний струм короткого замикання досягає 13,9 мА/см², а напруга холостого ходу — близько 0,725 В. Для ZnO як матеріалу електронного транспорту (ETM) отримано такі найкращі результати: загальна ефективність $\eta \approx 7{,}71\%$, коефіцієнт заповнення $FF \approx 63{,}18\%$, струм короткого замикання $J_{SC} \approx 13{,}9$ мА/см², напруга холостого ходу $V_{OC} \approx 0{,}725$ В. Чутливість та детектувальна здатність змодельованого фотодетектора становлять $R = 0{,}23$ А/Вт і $D^* = 1{,}1 \cdot 10^{10}$ Джонс. Для покращення продуктивності фотодетекторів було досліджено вплив товщини шарів, концентрації неглибоких донорів та густини дефектів. Отримані результати моделювання свідчать про перспективність подальших досліджень у галузі оптоелектронних пристроїв на основі ZnO.

Ключові слова: фотоелемент, фотодетектор, числове моделювання, матеріал електронного транспорту (ETM), ZnO, гетероструктура, програма SCAPS-1D.

Відомості про авторів

Ігор Вірт, докт. фіз.-мат. наук, професор, Дрогобицький державний педагогічний університет імені Івана Франка, Україна;
e-mail: isvirt@dspu.edu.ua;
ORCID: https://orcid.org/0000-0001-7200-6055

Іван Падалка, аспірант, Дрогобицький державний педагогічний університет імені Івана Франка, Україна;
e-mail: ivan.padalka@dspu.edu.ua;
ORCID: https://orcid.org/0009-0007-4071-5878

About the authors

Ihor Virt, Dr. Sc, Professor, Ivan Franko State Pedagogical University of Drohobych, Ukraine;
e-mail: isvirt@dspu.edu.ua;
ORCID: https://orcid.org/0000-0001-7200-6055

Ivan Padalka, Grad. Student, Ivan Franko State Pedagogical University of Drohobych, Ukraine;
e-mail: ivan.padalka@dspu.edu.ua;
ORCID: https://orcid.org/0009-0007-4071-5878